

# Accelerated cell divisions drive the outgrowth of the regenerating spinal cord in axolotls

Fabian Rost<sup>1†</sup>, Aida Rodrigo Albors<sup>2,3,4†</sup>, Vladimir Mazurov<sup>3,4</sup>, Lutz Brusch<sup>1,5</sup>, Andreas Deutsch<sup>1,5</sup>, Elly M. Tanaka<sup>3,4‡\*</sup> and Osvaldo Chara<sup>1,6‡\*</sup>

<sup>1</sup> Center for Information Services and High Performance Computing, Technische Universität Dresden, Dresden, Germany

<sup>2</sup> Present address: Division of Cell & Developmental Biology, School of Life Sciences, University of Dundee, Dundee, United Kingdom

<sup>3</sup> Deutsche Forschungsgemeinschaft – Center for Regenerative Therapies Dresden, Dresden, Germany

<sup>4</sup> Max Planck Institute of Molecular Cell Biology and Genetics, Dresden, Germany

<sup>5</sup> Center for Advancing Electronics Dresden (cfaed), 01062 Dresden, Germany

<sup>6</sup> Systems Biology Group (SysBio), Institute of Physics of Liquids and Biological Systems, National Scientific and Technical Research Council (CONICET) and University of La Plata, La Plata, Argentina

† Co-first authorship

‡ Co-last authorship

\* Corresponding authors

Corresponding authors:

Osvaldo Chara

Center for Information Services and High Performance Computing, Technische Universität Dresden,  
Nöthnitzer Straße 46, 01187 Dresden, Germany  
Tel. +49 351 463-38780  
E-mail: [osvaldo.chara@tu-dresden.de](mailto:osvaldo.chara@tu-dresden.de)

Systems Biology Group (SysBio), Institute of Physics of Liquids and Biological Systems (IFLySIB),  
National Scientific and Technical Research Council (CONICET) and University of La Plata  
Calle 59 N 789, 1900 La Plata, Argentina  
Tel. +54 221 4233283 Ext: 26  
E-mail: [ochara@iflysib.unlp.edu.ar](mailto:ochara@iflysib.unlp.edu.ar)

Elly Tanaka

Deutsche Forschungsgemeinschaft – Center for Regenerative Therapies Dresden (CRTD)  
Fetscherstraße 105, 01307 Dresden, Germany  
Tel. +49 351 458-82000  
E-mail: [elly.tanaka@crt-dresden.de](mailto:elly.tanaka@crt-dresden.de)

## Abstract

Axolotls are unique in their ability to regenerate the spinal cord. However, the mechanisms that underlie this phenomenon remain poorly understood. Previously, we showed that resting stem cells in the axolotl spinal cord revert to a molecular state resembling embryonic neuroepithelial cells and functionally acquire rapid proliferative divisions during regeneration. Here we refine in space and time this increase in cell proliferation during regeneration, and identify a dynamic high-proliferation zone in the regenerating spinal cord. By tracking sparsely-labeled cells, we quantify cell influx into the regenerate. Taking a mathematical modelling approach, we integrate these quantitative biological datasets across cellular and tissue level to provide a mechanistic and quantitative understanding of regenerative spinal cord outgrowth. We find that the acceleration of the cell cycle is necessary and sufficient to drive the outgrowth of the regenerating spinal cord in axolotls.

## Introduction

Neural stem cells exist in the spinal cord of all vertebrates, but only in salamanders these cells are mobilized efficiently to resolve spinal cord injuries (Becker & Becker, 2015; Tanaka and Ferretti, 2009). In axolotls, this is best exemplified following tail amputation, when cells adjacent to the cut end regrow a fully functional spinal cord (Holtzer, 1956; Mchedlishvili *et al.*, 2007). Despite the regenerative potential of axolotl neural stem cells, little was known about the molecular changes occurring upon these cells and the changes in cell behavior that lead to the fast expansion of the neural stem cell pool during regeneration.

In our previous study, we looked at spinal cord regeneration at the molecular and cellular level. There, we found that resident SOX2<sup>+</sup> neural stem cells re-activate an embryonic-like gene expression program following tail amputation (Rodrigo Albors *et al.*, 2015). Part of this program involves the re-establishment of planar cell polarity (PCP) signaling, the downregulation of pro-neural genes, and upregulation of proliferation-promoting genes. In line with these gene expression changes, we also found that regenerating neural stem cells speed up their cell cycle, and switch from neuron-generating to proliferative cell divisions. PCP turned out to be key for the efficient and orderly expansion of the regenerating spinal cord at least in part by instructing cells to divide along the growing axis. However, besides oriented cell division, whether other cell mechanisms such as

convergence and extension or neural stem cell recruitment are required for the rapid expansion of the regenerating spinal cord remained unknown.

In this follow-up study we investigate how different cell mechanisms contribute to the elongation of the regenerating spinal cord in the axolotl. To address this question we apply a quantitative modeling approach to causally link previous (Rodrigo Albors *et al.*, 2015) and new datasets to the time-course of spinal cord outgrowth. Particularly, we calculate neural stem cell density from previous measurements (Rodrigo Albors *et al.*, 2015) to show that convergence and extension are negligible. We make use of cell proliferation-related measurements along the anterior-posterior axis (AP) of the spinal cord (Rodrigo Albors *et al.*, 2015) to identify a high-proliferation zone that extends 800  $\mu\text{m}$  anterior to the amputation plane, and calculate changes in cell cycle kinetics within this zone. By tracing sparsely-labelled cells, we also determine the cell influx into the regenerating spinal cord. Finally, we set up a mathematical model of spinal cord outgrowth that incorporates cell proliferation, neural stem cell activation and cell influx. Using this model, we test the contribution of each of these cell mechanisms to the regenerative spinal cord outgrowth. Comparing the predictions of the model with experimental data of tissue outgrowth we show that while cell influx and the activation of quiescent neural stem cells play a minor role, the acceleration of the cell cycle in the high-proliferation zone is necessary and sufficient to explain the observed regenerative outgrowth.

## Results

### The regenerating spinal cord grows with increasing velocity

In order to refine the outgrowth time-course of the regenerating spinal cord, we measured the spinal cord outgrowth in individual axolotls during the first 8 days of regeneration (Figure 1A, Figure 1 – figure supplement 1 and Supplementary file 1). Initially, the regenerating spinal cord extended slowly to a mean outgrowth of  $0.45 \pm 0.04$  mm at day 4 (Figure 1B). Thereafter, the spinal cord grew faster, reaching an outgrowth of  $2.3 \pm 0.1$  mm by day 8.

# **The density of neural stem cells stays constant along the AP axis of the regenerating spinal cord**

To explain the outgrowth time-course of the regenerating spinal cord in terms of underlying cellular activities, we first set out to translate tissue outgrowth into cell numbers. To quantitatively investigate neural stem cell arrangement in space and time, we revisited our previously published dataset of the number of SOX2<sup>+</sup> cells per cross section in uninjured and regenerating spinal cords (Figure 2A and see Materials and methods) (Rodrigo Albors *et al.*, 2015). We found that the number of SOX2<sup>+</sup> cells per spinal cord cross section is constant along the AP axis in both uninjured and regenerating samples at any time (Figure 2B,B' and Figure 2 – figure supplement 1). We also found that the number of SOX2<sup>+</sup> cells per cross section spatially averaged along the AP axis is constant during regeneration time (Figure 2C and see Materials and methods). On average,  $30.4 \pm 0.6$  SOX2<sup>+</sup> cells make up the circumference of the axolotl spinal cord. Since the length of SOX2<sup>+</sup> cells along the AP axis does not change during regeneration ( $l_c = 13.2 \pm 0.1 \mu\text{m}$ ) (Rodrigo Albors *et al.*, 2015), the density of cells along the AP axis is spatially homogeneous and equal to  $2.3 \pm 0.6$  cells /  $\mu\text{m}$  (Figure 2A).

Taken together, these findings allow us to exclude cell mechanisms such as cell shape changes as well as convergence and extension, which leads to the narrowing and lengthening of tissues, as driving forces of the polarized spinal cord growth in the axolotl. Instead, constant neural stem cell density implies an increasing neural stem cell number during regeneration. This suggests that the expansion of the regenerating neural stem cell pool relies on proliferation-related mechanisms.

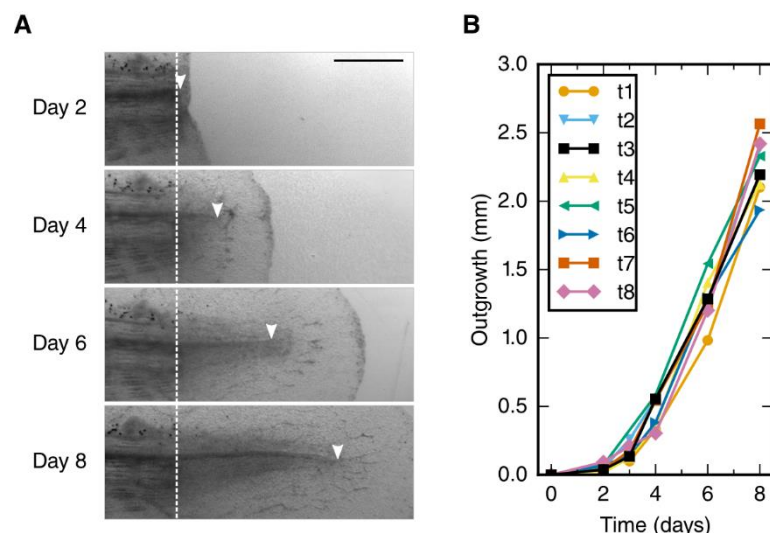


**Figure 1. Spinal cord outgrowth time-course during regeneration (A)** Representative images of a regenerating spinal cord after tail amputation (individual time-lapse images are in Figure 1 – figure supplement 1). The white dashed line marks the amputation plane. The arrowheads mark the tip of the regenerating spinal cord. Scale bar, 1mm. **(B)** Spinal cord outgrowth time-course during the first 8 days after amputation ( $n = 8$  axolotls).

# **Cell proliferation increases within an 800 $\mu$ m zone anterior to the amputation plane in 4-day regenerates**

To determine spatial and temporal changes in cell proliferation during regeneration, we calculated different cell proliferation parameters along uninjured and regenerating spinal cords. In our previous study, we quantified the number of proliferating cells and the number of mitotic cells using an antibody against proliferating cell nuclear antigen (PCNA) and Hoechst DNA stain (Rodrigo Albors *et al.*, 2015). Here, we used these datasets to estimate the growth fraction, i.e. the fraction of PCNA<sup>+</sup>/SOX2<sup>+</sup> cells (proliferating cells), and the mitotic index, i.e. the fraction of proliferating cells undergoing mitosis (see Materials and methods). Although neither PCNA<sup>+</sup>/SOX2<sup>+</sup> cells nor mitotic cells showed any evident spatial pattern along the AP axis in uninjured animals (Figure 2 D, points), they showed a tendency to increase posteriorly from day 4 (Figure 2 D', points). To elucidate whether proliferation was patterned along the AP axis during the time of regeneration, we tested the data with a mathematical model of two spatially homogeneous zones characterized by their growth fraction and mitotic index and separated by a border that we call the *switchpoint* (Figure 2E, E'). We reasoned that in the absence of an AP pattern of cell proliferation the two zones would be indistinguishable; while if cell proliferation would be locally increased, the model would allow us to determine the magnitude and

the location of the increased cell proliferation. For a given growth fraction and mitotic index, the model predicts the expected number of proliferating cells and mitotic cells per cross section (Figure 2 – figure supplement 2). Hence, we fitted the model to the cell number datasets of uninjured and regenerating spinal cords at day 3, 4, 6 and 8 after amputation (Figure 2E,E', Figure 2 – figure supplement 3 and Figure 2 – figure supplement 4) to determine the growth fraction, the mitotic index, and the switchpoint for each time point (Figure 2F-F''). Not surprisingly, we found that in the uninjured spinal cord the growth fraction and the mitotic index in the two modeled zones are not significantly different (Figure 2E,F,F' and Figure 2 – figure supplement 3). Similarly, at day 3 there are no significant differences between the two zones (Figure 2F,F' and Figure 2 – figure supplement 3). In contrast, the growth fraction and the mitotic index are higher in the posterior zone from day 4 onward (Figure 4E', F, F' and Figure 2 – figure supplement 3). These findings reveal that a high-proliferation zone emerges in the regenerating spinal cord at day 4. At this time point, the switchpoint between the two zones is located  $800 \pm 100 \mu\text{m}$  anterior to the amputation plane, but shows the tendency to shift posteriorly at later time points as the regenerating spinal cord grows (Figure 2F'').

Next, we combined the mitotic index measurements with our previous cell cycle length estimates (Rodrigo Albors *et al.*, 2015) to establish how the proliferation rate changes during regeneration (Figure 2G and see Material and methods). We find that the proliferation rate is  $0.06 \pm 0.02$  per day in the uninjured spinal cord which corresponds to a cell cycle length of  $10 \pm 4$  days (Figure 2 – figure supplement 5). The proliferation rate is similar at day 3. However, at day 4 the proliferation rate increases to about 0.15 per day corresponding to a cell cycle length of about 5 days and the proliferation rate remains that high until day 8.

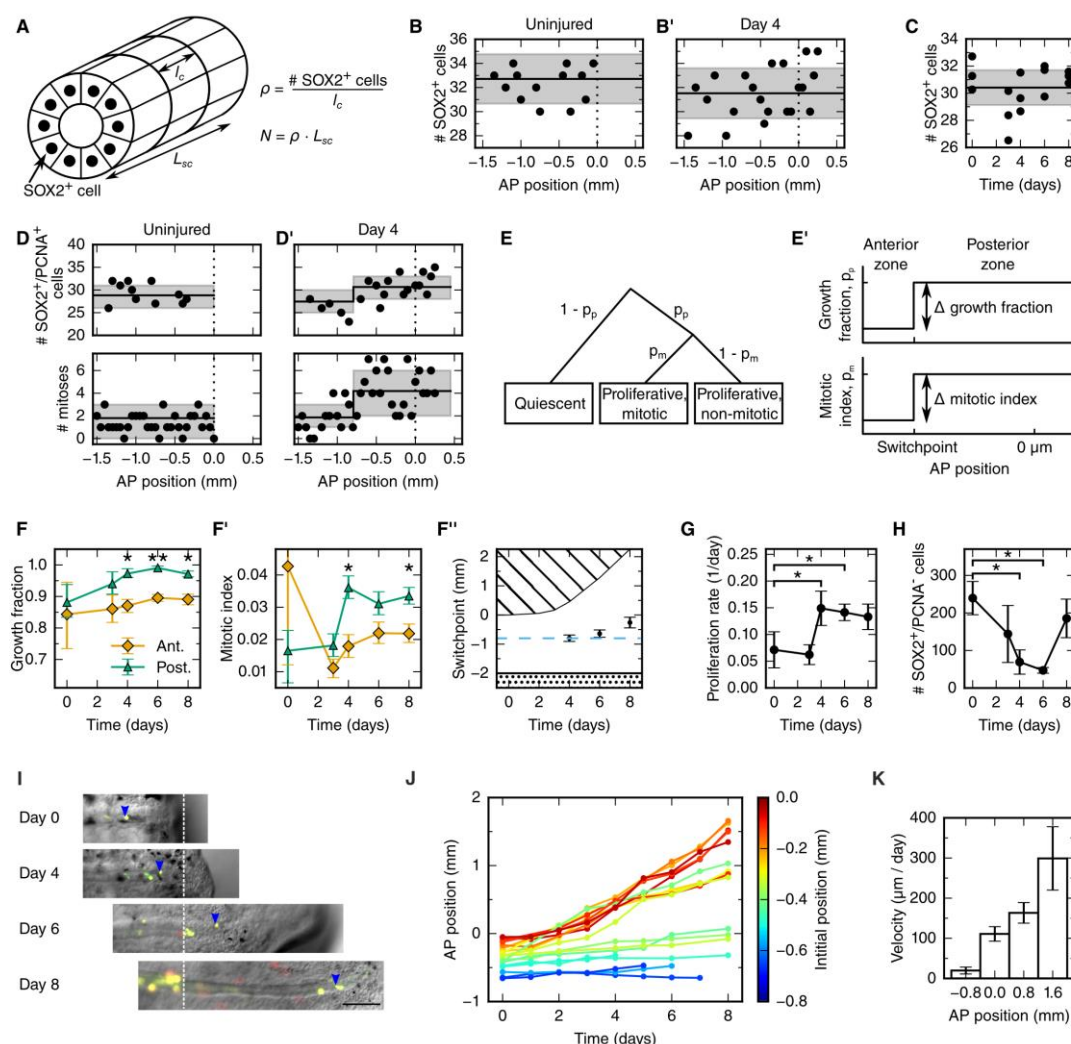


**Figure 2. Cellular mechanisms underlying spinal cord outgrowth.** (A) Sketch of measurements taken to estimate the density and total number of neural stem cells (nuclei, black dots) in the axolotl spinal cord. The density of SOX2<sup>+</sup> cells,  $\rho$ , is the ratio of the number of SOX2<sup>+</sup> cells per cross section (# stem cells) and the mean AP cell length,  $l_c$ . The density of SOX2<sup>+</sup> cells is the proportionality constant between the total number of stem cells in a zone along the spinal cord with zone length,  $L_{sc}$ . (B,B') Number of SOX2<sup>+</sup> per cross section along the AP axis of a selected uninjured (B) and a selected day 4-regenerating spinal cord (B'). Black line and grey region indicate the mean number of SOX2<sup>+</sup> cells and the standard deviation, respectively. Plots for all individual axolotls in Figure 2 – figure supplement 1. (C) Spatial average of the number of SOX2<sup>+</sup> cells per cross section of individual axolotls against time (black dots). Black line and gray region indicate the mean number of SOX2<sup>+</sup> cells and the standard deviation of all animals, respectively. (D,D') Number of SOX2<sup>+</sup>/PCNA<sup>+</sup> cells per cross section (upper panel) and mitotic cells per section (lower panel) along the AP axis in a selected uninjured (D) and a selected day 4-regenerating spinal cord (D'). Black line and the gray region show the expected number and the 68% confidence belt for the best fit of the model with two spatial proliferation zones, respectively. Plots for all animals in Figure 2 – figure supplement 3. (E) Possible cell states in the two spatial proliferation zones model used to analyze the spatial cell proliferation dataset (D,D').  $p_p$ , probability that a cell is proliferative, otherwise quiescent.  $p_m$ , probability that a proliferative cell undergoes mitosis. (E') The model assumes two proliferation zones. The location of the border between zones is called *switchpoint*. (F-F') Results of model fitting for growth fraction (F) and mitotic index time-course (F') in the anterior (orange diamonds) and posterior (green triangles) zone. Error bars indicate the 68% credibility interval. (F'') Black dots mark the switchpoint. Blue dashed line marks 800  $\mu$ m anterior to the amputation



plane. The dashed region marks the space outside of the embryo, the dotted region marks the unaffected part of the embryo. **(G)** Proliferation rate time-course in the high-proliferation zone. **(H)** Total number of SOX2<sup>+</sup>PCNA<sup>-</sup> cells in the high-proliferation zone (mean  $\pm$  linearly propagated 1- $\sigma$  error). **(I)** Selected time-lapse images of clone (blue arrowhead) tracking during spinal cord regeneration. Dashed line marks the amputation plane. **(J)** Tracking of 19 clones along the AP axis during regeneration. Clone trajectories are color coded by their initial position. **(K)** Clone velocities at different positions along the AP axis.

## Quiescent neural stem cells re-enter the cell cycle during regeneration

Two possible scenarios could lead to the observed increased growth fraction in the high-proliferation zone: the activation of quiescent neural stem cells, or the dilution of quiescent cells by the expansion of the proliferating cell population. If quiescent cells were activated, the total number of quiescent cells in the high-proliferation zone would decrease. We estimated the total number of quiescent cells in the high-proliferation zone from the mean number of SOX2<sup>+</sup>PCNA<sup>-</sup> cells per cross section, the mean AP cell length, and the outgrowth time-course (see Materials and methods). The number of SOX2<sup>+</sup>PCNA<sup>-</sup> cells drops from  $180 \pm 30$  at day 0 to  $23 \pm 13$  at day 6 (Figure 2H) which means that quiescent SOX2<sup>+</sup> cells get activated and re-enter the cell cycle upon injury. The number of quiescent SOX2<sup>+</sup> cells appears to increase again at day 8, when cells resume neurogenesis (Rodrigo Albors *et al.*, 2015).

## Cells move faster the closer they are to the tip of the regenerate

Cell movement could also contribute to regenerative spinal cord growth. To investigate whether anterior neural stem cells move into the high-proliferation zone, we followed individual cells during regeneration. For that, we co-electroporated cytoplasmic GFP and nuclear mCherry plasmids at very low concentration to achieve sparse labelling of cells and tracked them daily during the first 8 days of regeneration (Figure 2I and see Materials and methods). We found that labelled cells preserve their original spatial order: cells located close to the amputation plane end up at the posterior end of the regenerated spinal cord (Figure 2J). Most-anterior cells, however, almost do not change their position. From the clone trajectories, we calculated the mean clone velocity at different positions along the AP axis (Figure 2K and see Materials and methods). Clones initially located 800  $\mu$ m anterior to the amputation plane move slowly, with a velocity of  $20 \pm 9$   $\mu$ m/day. In contrast, the more posterior a clone is, the faster it moves.



# Cell proliferation drives the outgrowth of the regenerating spinal cord

Above we showed that cell density is constant along the AP axis of the regenerating spinal cord (Figure 2B and C). The spinal cord must therefore grow as a result of increasing cell numbers. In line with this, we found a high-proliferation zone, first spanning from 800  $\mu\text{m}$  anterior to the amputation plane, and showed that the increase in cell proliferation is due to both (i) the acceleration of the cell cycle and (ii) the activation of quiescent stem cells. Based on our finding of cell flow during regeneration (Figure 2J and Figure 2K), the influx of cells into the regenerating spinal cord could also contribute to increasing the cell numbers in the regenerating spinal cord (Figure 3A). To assess the contribution of these cell mechanisms to the spinal cord outgrowth time-course, we used a quantitative mathematical modeling framework (Greulich & Simons 2016; Rué & Martinez Arias, 2015; Oates *et al.*, 2009). Assuming that cells entering the high-proliferation zone at the switchpoint acquire the features of high-proliferative cells via activation, we formalized the influence of those cellular mechanisms on the total number of proliferating and quiescent SOX2<sup>+</sup> cells in the high-proliferation zone (see Materials and methods, equations (3) and (4)). Making use of the constant cell density along the spinal cord we rewrote this cell number model as a model for spinal cord outgrowth,  $L$ , and growth fraction,  $GF$ :

$$\frac{dL}{dt} = \overbrace{r(t) (L + L_0) GF}^{\text{divisions of proliferating cells}} + \overbrace{\tilde{v}}^{\text{influx of cells into the high-proliferation zone}}, \quad L(t = 0) = 0, \quad (1)$$

$$\frac{dGF}{dt} = \underbrace{(1 - GF) k}_{\text{activation of quiescent SOX2+ cells}} + \underbrace{(1 - GF) r(t) GF}_{\text{dilution of quiescent SOX2+ cells in the expanding pool of proliferating cells}}, \quad GF(t = 0) = GF_0 \quad (2)$$

where  $L_0 = 800 \mu\text{m}$  is the length of the high-proliferation zone,  $GF_0$  is the growth fraction in uninjured tails,  $r(t)$  is the proliferation rate at time  $t$ ,  $v$  is the velocity of cells 800  $\mu\text{m}$  anterior to the amputation plane, and  $k$  is the cell cycle entry rate. As we determined the proliferation rate time-course  $r(t)$  (Figure 2G), the initial growth fraction  $G_0$  (Figure 2F) and the influx velocity  $v$  (Figure 2K), only the cell cycle entry rate  $k$  is unknown. By fitting the model to the experimental growth fraction data from day 0 to day 6 (Figure 3B), we determined this parameter as  $k = 0.2 \pm 0.1 \text{ day}^{-1}$ . Strikingly, the model predicts a spinal cord outgrowth time-course that recapitulates the experimental data (Figure 3C). This fit-free agreement shows that acceleration of the cell cycle, activation of quiescent neural stem cells, and an influx of cells quantitatively explain the observed time course of spinal cord outgrowth.

To quantitatively determine the contribution of each cell mechanism we switched them off one by one *in silico*. Switching off the acceleration of the cell cycle leads to an outgrowth of less than 1.7 mm by day 8 due to the basal proliferation rate in the uninjured spinal cord, the influx of cells towards the amputation plane and the activation of quiescent neural stem cells (Figure 3D). This underestimates the experimental outgrowth which implies that the acceleration of the cell cycle is necessary to drive spinal cord outgrowth. In contrast, switching off cell influx does nearly not affect spinal cord outgrowth, implying that cell influx is not a major driver of regenerative outgrowth (Figure 3E). Similarly, switching off the activation of quiescent stem cells has only a small effect on regenerative spinal cord outgrowth (Figure 3F). Interestingly, when both, cell influx and cell activation are switched off the experimental spinal cord outgrowth time-course is correctly predicted, implying that acceleration of the cell cycle is sufficient to drive the regenerative process (Figure 3G).

Taken together, our model shows that the acceleration of the cell cycle in cells that were already proliferating in the uninjured spinal cord is necessary and sufficient to explain the observed spinal cord outgrowth.

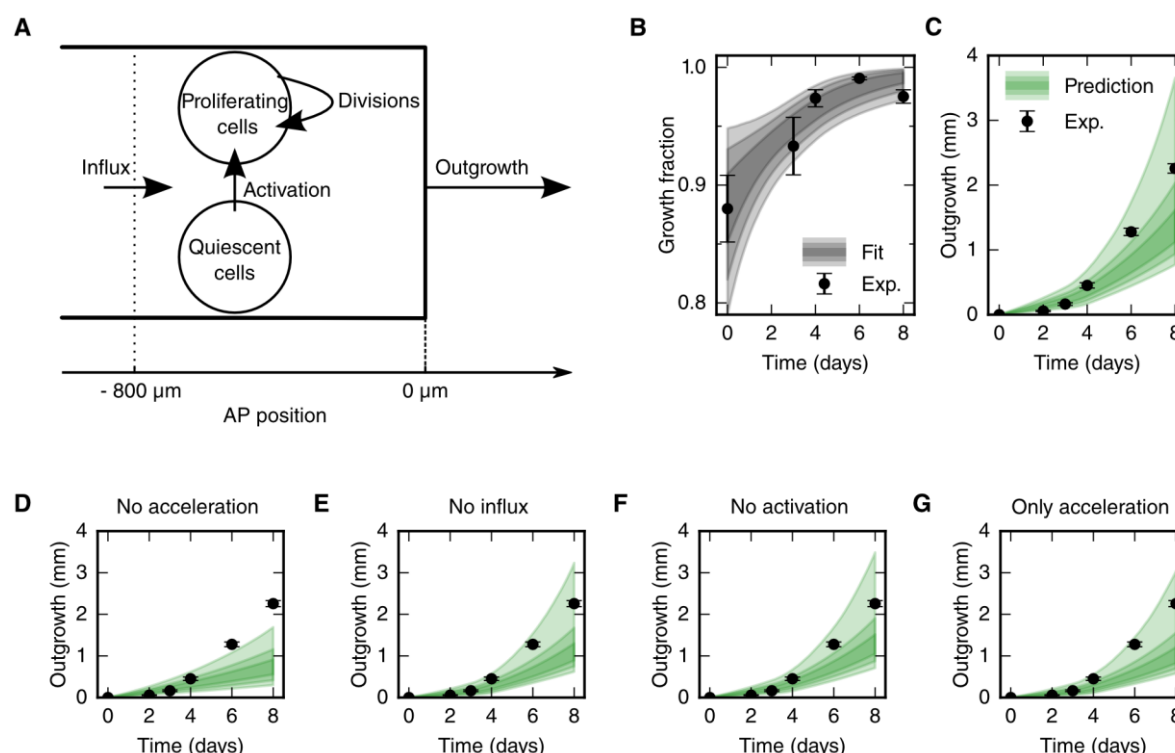


**Figure 3. Mechanistic model of spinal cord outgrowth.** (A) Sketch of cell mechanisms included in the model: cell proliferation, quiescent cell activation, and cell influx into the 800 μm high-proliferation zone. (B) Growth fraction time-course of the SOX2<sup>+</sup> cell population in the high-proliferation zone as observed (black dots) and fitted by the model (grey shaded areas, from darker to lighter, 68%, 95% and 99.7% confidence intervals of the model prediction). (C) Spinal cord outgrowth during the first eight days of regeneration as observed (black dots,  $n = 8$

axolotls) and predicted by the model (green shaded areas). The model prediction is in agreement with the experimental data. **(D-G)** Prediction of spinal cord outgrowth for four model scenarios with selected mechanisms switched off (green shaded areas). Black dots show the same experimental data as in panel (C). (D) The acceleration of the cell cycle is switched off. Hence, the proliferation rate is fixed to the basal proliferation rate of uninjured animals. (E) Cell influx is switched off ( $v = 0$ ). (F) Quiescent cell activation is switched off ( $k = 0$ ). (G) Cell influx and quiescent cell activation are switched off ( $k = 0$ ,  $v = 0$ ). Corresponding predictions for growth fraction in Figure 3 – supplementary figure 1.

## Discussion

The spinal cord tissue size and architecture is faithfully restored after tail amputation in axolotls. This unique regenerative capability relies on the neural stem cells surrounding the central canal of the spinal cord. These cells re-activate an embryonic gene expression program that implements PCP signaling to make possible the increase in cell proliferation while maintaining a tube-like structure (Rodrigo Albers *et al.*, 2015). However, whether other cellular mechanisms (such as convergence and extension, activation of quiescent neural stem cells or influx of cells) could contribute as well to the regenerated spinal cord outgrowth remained unknown.

Here, we combined detailed quantitative datasets with mathematical modeling to dissect the cell mechanisms that underlie regenerative spinal cord outgrowth in axolotls. We found that the response to injury involves (i) changes in the cell proliferation rate, (ii) activation of quiescent cells, and (iii) cell influx into the regenerating spinal cord, while maintaining a surprisingly organized neural stem cell-scaffold. Modeling the contribution of each of these mechanisms to tissue outgrowth upon regeneration, we uncovered that the acceleration of the cell cycle is the main driver of regenerative spinal cord outgrowth in axolotls.

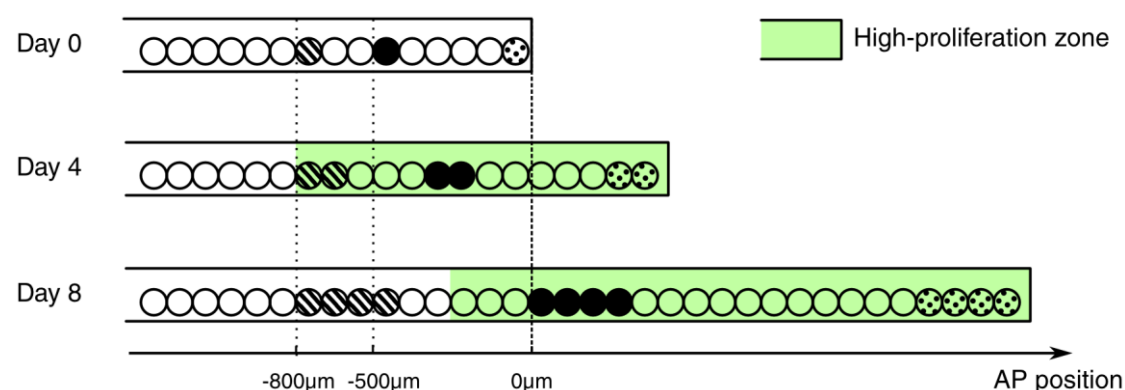


**Figure 4. Conceptual model of spinal cord growth during regeneration.** Only one row of stem cells is shown

as circles and three cell clones are marked with different patterns (striped, black and dotted). In the uninjured spinal cord (Day 0), cells divide at a slow, basal proliferation rate (white background). From day 4 after amputation, cells speed up their cell cycle and the growth fraction increases, within a high-proliferation zone that initially extends 800  $\mu\text{m}$  anterior to the amputation plane (green background). The density of neural stem cells along the spinal cord stays constant and spinal cord outgrowth is achieved by an increase in the total number of neural stem cells. Cell proliferation in the high-proliferation zone is necessary and sufficient to provide this increase in cell numbers. Dividing cells might push cells posteriorly. The more posterior a cell is the more cells anterior to that cell divide and push the cell making it move faster: While an anterior clone (striped) hardly moves, clones in the center of the high proliferation zone (black) move faster. Clones that start at the amputation plane (dotted) stay at the tip of the regenerating spinal cord and move fastest.

Increased proliferation of SOX2<sup>+</sup> cells upon spinal cord injury is a common feature among vertebrates (Becker & Becker, 2015). In zebrafish (Hui *et al.*, 2010; Hui *et al.*, 2015), *Xenopus* (Gaete *et al.*, 2012), mouse (Lacroix *et al.*, 2014) and axolotl (this work, Rodrigo Albors *et al.* 2015, Holtzer, 1956) traumatic spinal cord injury triggers a long-range wave of increased cell proliferation. It is however clear that although the potential to replace lost cells or tissue exists in other species, they are not as efficient as axolotls resolving spinal cord injuries. A more comprehensive characterization of cell proliferation responses is thus needed to understand fundamental differences between species with different regenerative capabilities. In our previous study, we uncovered that spinal cord stem cells speed up their cell cycle during regeneration (Rodrigo Albors *et al.*, 2015). Performing detailed quantifications in the axolotl, we were now able to delineate a high-proliferation zone that initially spans from the 800  $\mu\text{m}$  adjacent to the amputation plane to the regenerating tip, and later shifts posteriorly, as the spinal cord regrows. Although quiescent neural stem cells enter the cell cycle during regeneration, we demonstrate that the observed increase in proliferation is primarily due to the acceleration of the cell cycle within the regenerating pool of neural stem cells. By performing experiments *in silico* using our mechanistic model of spinal cord regeneration, we demonstrated that this acceleration of the cell cycle is necessary and sufficient to explain the observed spinal cord outgrowth. In agreement with this, Sox2-knockout spinal cords fail to regrow upon tail amputation, due to the inability of Sox2-knockout cells to ‘change gears’ in response to injury (Fei *et al.*, 2014). Indeed, while Sox2-knockout cells express PCNA like their SOX2<sup>+</sup> counterparts and are therefore able to proliferate, their lower incorporation of the thymidine analog 5-ethynyl-2'-deoxyuridine (EdU) indicates that they cannot speed up their cell cycle (Fei *et al.*, 2014). Our findings highlight the importance of careful quantification of cell proliferation and of mathematical modeling to understand the mechanisms

of regeneration. Moreover, our detailed spatial and temporal characterization of cell proliferation might help to focus the search for key signals that might be operating in the high-proliferation zone to speed up the cell cycle of regenerative neural stem cells. It will be interesting to see whether the expression of AxMLP, the recently identified regeneration-initiating factor in axolotls (Sugiura *et al.*, 2016), correlates in time and space with the high-proliferation zone.

By tracking cells during regeneration, we found that cells move along the AP axis of the spinal cord but maintain their relative position: cells move faster the closer they are to the amputation plane (Figure 2J,K). In line with earlier work (Mchedlishvili *et al.*, 2007), we found that cells initially located within the 500  $\mu\text{m}$  anterior to the amputation plane move fast enough to contribute to the regenerated spinal cord; while cells outside this zone move slower, and cells at 800  $\mu\text{m}$ , the border of the high-proliferation zone, almost do not move. This is consistent with a model in which cells are passively displaced, pushed by more anterior dividing cells. In this model, the more posterior a cell is the more cells anterior to that cell divide and the stronger is the push, making the cell move faster (Figure 4). Importantly, the proliferative response extends beyond the 500  $\mu\text{m}$  anterior to the amputation plane that gives rise to the regenerated spinal cord (Mchedlishvili *et al.*, 2007). In the light of this model, it is plausible that cells in the posterior 500  $\mu\text{m}$  of the high-proliferation zone produce the regenerated spinal cord posterior to the amputation plane. Simultaneously cells from the anterior 300  $\mu\text{m}$  of the high-proliferation zone replenish and push out the posterior 500  $\mu\text{m}$ .

A notable finding of this study is that the increase in cell numbers during regeneration is tightly regulated so that the regenerating spinal cord extends while maintaining constant cell density and its proper tube-like structure. This tube-like structure made up almost entirely of neural stem cells might be essential to act as a scaffold for rebuilding the complete spinal cord tissue architecture. Previously, we showed that the activation of PCP signaling within the source zone instructs cells to divide along the growing axis of the spinal cord and is key for effective spinal cord regeneration. This work highlights the importance of orderly and directed expansion of the neural stem cell pool for efficient spinal cord regeneration.

Together, our findings provide a quantitative mechanistic understanding of the cellular mechanisms that drive complete spinal cord regeneration in axolotls. By performing a quantitative modeling approach combined with quantitative experimental data, we found that axolotl spinal cord outgrowth is driven by the acceleration of the cell cycle in a pool of SOX2<sup>+</sup> neural stem cells restricted

in space and time. Whether this peculiar spatiotemporal proliferative pattern is unique to the axolotl and how this correlates with injury-induced signals remain to be elucidated.

## Materials and methods

### Axolotls

Axolotls, *Ambystoma mexicanum*, from 2 to 3 cm in length snout-to-tail were used for experiments. Axolotls were kept in tap water in individual cups and fed daily with *Artemia*. Before any manipulation or imaging, axolotls were anaesthetized in 0.01% benzocaine. The axolotl animal work was performed under permission granted in animal license number DD24-9168.11-1/2012-13 conferred by the Animal Welfare Commission of the State of Saxony, Germany (Landesdirektion Sachsen).

### Measurement of spinal cord outgrowth

Images of regenerating tails were acquired on an Olympus SZX16 stereomicroscope using the Cell<sup>^</sup>F software by Olympus. Spinal cord outgrowth was measured from bright field images in Fiji. First, the amputation plane which is clearly visible in the myotome was marked with a line. Then, the length between the intersection of the amputation plane with the spinal cord and the spinal cord tip was measured with Fiji's line tool.

### Cell count data

The cell count data of SOX2<sup>+</sup> and SOX2<sup>+</sup>/PCNA<sup>+</sup> cells per cross section and mitotic cells in 50  $\mu$ m sections were taken from Rodrigo Albors *et al.*, 2015.

### Spatial model of cell counts to analyze the spatiotemporal pattern of proliferation

To test whether the SOX2<sup>+</sup> cells per cross section showed a spatial pattern along the AP axis or not, we used three different methods (Figure 2B,B', Supplementary Figure 1). First, it was tested if the cell count data linearly depends on spatial position along the AP axis using Bayesian inference (see Supplementary notebook "Constant Density"). The slope was always smaller than 0.13 cells / mm and only significantly different from 0 ( $p < 0.05$ ) for 4 of the 15 replicates. Second, a model of two

spatially homogeneous zones was fitted to the data using Bayesian inference (see Supplementary notebook “Constant Density”). Here, only 4 of the 15 replicates showed a significant difference in density between the two zones ( $p < 0.05$ ). These first two methods indicated that, for an average animal, there is no significant change of the number of SOX2<sup>+</sup> cells per cross section along the AP axis. Third, the data was collapsed ignoring the spatial position, and the resulting cell count histogram was tested for being a normal distribution using the SciPy function `scipy.stats.normaltest` (D’agostino, 1971; D’agostino and Pearson, 1973). Only for one of the replicates the null hypothesis could be rejected ( $p < 0.05$ ), hence SOX2<sup>+</sup> cell density in an average animal was considered spatially homogeneous with Gaussian noise in this study.

For each replicate the mean number of SOX2<sup>+</sup> cells per cross section averaged over all measurements along the AP axis was calculated. To access whether there was a significant change in this mean number, the replicates were grouped according to their time post amputation. A one-way ANOVA-test showed no significant differences among the groups ( $p = 0.08$ , see Supplementary Notebook “Constant Density”).

## Analysis of proliferation count data

The counts of SOX2<sup>+</sup> cells, SOX2<sup>+</sup>/PCNA<sup>+</sup> cells and mitotic cells were analyzed by fitting a mathematical model of two adjacent spatial proliferation zones to the data of each time point (Figure 2E,E', Figure 2 – figure supplement 3).

The model that predicts the number of SOX2<sup>+</sup>/PCNA<sup>+</sup> cells per cross section and the number of mitotic cells in three-dimensional (3D) 50  $\mu$ m sections based on the growth fraction and mitotic index was defined as follows: If the number of SOX2<sup>+</sup> cells for a specific cross section along the AP axis,  $N_S$ , had been measured, it was used for this section. If the data for the specific section was missing,  $N_S$  was computed by assuming that there is a constant expected number of SOX2<sup>+</sup> cells per cross section and that the deviations from the expected value follow a normal distribution. The mean and standard deviation of this normal distribution were estimated by the sample mean and standard deviation of the sample of the measured numbers of SOX2<sup>+</sup> cells per cross section for each replicate, respectively. The number of SOX2<sup>+</sup> in a cross section is independent from other cross sections. The state ‘Proliferative’, i.e. SOX2<sup>+</sup>/PCNA<sup>+</sup>, is independently assigned to each SOX2<sup>+</sup> cell with probability  $p_p$  or ‘Quiescent’ with probability  $1 - p_p$  (Figure 2D). Hence, for a given number of SOX2<sup>+</sup> cells in a



cross section,  $N_S$ , the number of SOX2<sup>+</sup>/PCNA<sup>+</sup> cells per cross section,  $N_P$ , follows a binomial distribution with  $N_S$  experiments and success probability  $p_p$ . Consequently, the expected growth fraction equals  $p_p$ . As the number of mitotic cells,  $N_M$ , in 3D 50  $\mu\text{m}$  sections was measured previously, we estimated the number of SOX2<sup>+</sup>/PCNA<sup>+</sup> cells also in a 3D 50  $\mu\text{m}$  section,  $N_{PS} = 50 \mu\text{m}/l_{\text{cell}} \cdot N_P$ , where  $l_{\text{cell}} = 13.2 \pm 0.1 \mu\text{m}$  is the mean AP length of SOX2<sup>+</sup> cells (Rodrigo Albors *et al.*, 2015). Assuming that the cell cycle position and hence the cell cycle phase of each cell is independent of all other cells, the state ‘Proliferative, mitotic’ is independently assigned to each SOX2<sup>+</sup>/PCNA<sup>+</sup> cell with probability  $p_m$  or ‘Proliferative, non-mitotic’ with probability  $1 - p_m$ . Hence, the number of mitotic cells per section,  $N_M$ , follows a binomial distribution with  $N_{PS}$  experiments and success probability  $p_m$ . Consequently, the expected mitotic index equals  $p_m$ . For given values of  $p_p$  and  $p_m$  the model gives a likelihood for the observed number of SOX2<sup>+</sup>/PCNA<sup>+</sup> cells per cross section and mitotic cells per 3D section that can be used to fit the model parameters. To reflect the assumption of two spatial proliferation zones,  $p_p$  and  $p_m$  have spatial dependencies in the form of step functions (Figure 2D’). Hence, there can be different growth fractions and mitotic indices for the anterior and the posterior zone, respectively. The spatial position of the border between the zones is another model parameter termed *switchpoint*. Furthermore, variability between replicates in the switchpoint is modeled as a normal distribution with standard deviation  $\sigma_{\text{switch}}$ . Likewise, variability in growth fraction and mitotic index between replicates is modeled with a normal distribution with spatially homogeneous standard deviations  $\sigma_{GF}$  and  $\sigma_{mi}$ , respectively. Hence, the resulting model to describe the cell count data of all replicates at a given time point has 8 parameters: the switch-point, growth fraction and mitotic index in the anterior zone and in the posterior zone, respectively, and the inter-replicate variabilities  $\sigma_{\text{switch}}$ ,  $\sigma_{GF}$  and  $\sigma_{mi}$ . Those parameters were estimated with Bayesian inference using uniform priors for uninjured animals and at 3, 4, 6 and 8 days. Fitting was performed using a Markov chain Monte Carlo algorithm implemented in pymc (Figure 2F-F’, Supplementary Figure 2,3, see also Supplementary notebook “step\_model\_fixed\_density\_fit\_per\_timepoint”). To verify the fitting procedure, test data were created by simulating our model with picked parameter values. These “true” parameter values were then found to be included in the 95% credibility intervals of the parameter values inferred from the test data with our fitting procedure.

## **Proliferation rate time-course**

The cell cycle length at day 6 was estimated previously using a cumulative 5-bromo-2'-deoxyuridine (BrdU) labelling approach (Rodrigo Albors *et al.*, 2015). For the sake of consistent methodology within the present study, the data were reanalyzed with bootstrapping using case resampling (see Supplementary Notebook "brdu\_bootstrapping\_day6"). In agreement with the previous analysis the cell cycle length was estimated as  $117 \pm 12$  h corresponding to a proliferation rate of  $0.21 \pm 0.02$  per day at 6 days after amputation.

As the mitotic index is proportional to the proliferation rate (Smith & Dendy, 1962), the mitotic index time-course in the high-proliferation zone was rescaled with the proliferation rate at day 6 to obtain the proliferation rate time-course:

$$r(t) = \frac{mi(t)}{mi(day\ 6)} r(day\ 6),$$

where  $r(t)$  is the proliferation rate at time  $t$ , and  $mi$  is the mitotic index. The mitotic index in the high-proliferation zone was estimated as described in (Rodrigo Albors *et al.*, 2015).

## **Axolotl spinal cord electroporation**

Axolotl larvae (2 cm snout-to-tail) were electroporated with a dual fluorescent reporter plasmid (cytoplasmic eGFP and nuclear Cherry). Cells were electroporated by cutting the tail of 2 cm-long larval axolotls and inserting a DNA-filled electrode into the spinal cord (Echeverri & Tanaka 2003). To transfect DNA into only a few cells, optimum electroporation conditions were three pulses of 50 V, 200 Hz and a length of 100 ms, applied using an SD9 Stimulator (Grass Telefactor, West Warwick, RI).

## **In vivo imaging of labeled cells in the spinal cord**

Axolotls with sparsely labelled cells in the spinal cord were amputated, leaving cells at different distances from the amputation plane. Regenerating axolotls were anaesthetized and imaged every 1-2 days by placing them on a cover slip. Labelled cells were imaged using a Zeiss Apotome A1 microscope.

## **Clone tracking**

The distance between the amputation plane and the anterior border of a clone was measured manually in each image using AxioVision microscopy software.

## Clone velocity

To estimate the mean velocity of clones at different spatial positions, the space along the AP axis was subdivided into 800  $\mu\text{m}$  bins. For each clone trajectory, the position measurements were grouped according to these bins. Groups containing less than 2 measurements were excluded. The average clone velocity for each group was estimated with linear regression. Then, the mean and standard deviation of the velocity of all the clones in a bin was calculated.

## Mechanistic model of spinal cord outgrowth

To simultaneously evaluate the importance of cell proliferation, cell influx and activation of quiescent cells in the outgrowth of the spinal cord we performed a data-driven modeling approach (Greulich & Simons 2016; Rué & Martinez Arias, 2015; Oates *et al.*, 2009). This approach allows to establish causal relationship between the individually quantified cellular processes and it has been previously employed to unravel the stem cell dynamics during spinal cord development in chick and mouse (Kicheva *et al.*, 2014). Although less frequent so far, modeling is more and more being used in the regeneration arena (Durant *et al.*, 2016; for an overview see Chara *et al.*, 2014). In this study we model the number of proliferating and quiescent cells in the high-proliferation zone by the following ordinary differential equations (Fig. 4A):

$$\frac{dN_p}{dt} = \overbrace{r(t) N_p}^{\text{cell divisions}} + \overbrace{k N_q}^{\text{activation}} + \overbrace{\frac{N_p}{N_p + N_q} v \rho}^{\text{influx}}, \quad N_p(t=0) = N_p^0 \quad (3)$$

$$\frac{dN_q}{dt} = -k N_q + \frac{N_q}{N_p + N_q} v \rho, \quad N_q(t=0) = N_q^0 \quad (4)$$

where  $N_p^0$  and  $N_q^0$  are the initial cell numbers in this zone,  $r(t)$  is the proliferation rate at time  $t$ ,  $v$  is the velocity of cells 800  $\mu\text{m}$  anterior to the amputation plane,  $\rho$  is the line density of cells along the AP axis and  $k$  is the quiescent cell activation rate. The factors  $N_{p/q} / (N_p + N_q)$  ensure that the influx of cells into the high-proliferation zone does not alter the growth fraction. As the density is constant one can write

$$\rho \cdot (L + L_0) = N_p + N_q, \quad (5)$$

where  $L$  is the outgrowth posterior to the amputation plane and  $L_0 = 800 \mu\text{m}$  is the high-proliferation zone length at  $t = 0$ . Using this relation and the definition of the growth fraction  $GF$ ,

$$GF = \frac{N_p}{N_p + N_q}, \quad (6)$$

the cell number model was reformulated as a model for outgrowth and growth fraction (see Results, equations (1) and (2)).

The assumption that the population mean model parameters can be used to estimate the population mean outgrowth time-course was used when simulating the model and interpreting results. The confidence intervals of the model prediction were estimated with a Monte Carlo approach using bootstrapping with a case resampling scheme (100,000 iterations). In each iteration we case-resampled the cell count data, the BrdU incorporation data and the clone trajectory data, and calculated the proliferation rate time-course, clone velocity at -800  $\mu\text{m}$  and initial growth fraction from this resampled data as described above. Then, in each iteration, these bootstrapped parameter values were used to estimate the activation rate  $k$  by fitting the model prediction of the growth fraction to the data (Fig. 4B). The growth fraction measurement of day 8 was excluded from the fit because its precise value would only affect the model prediction after this day. Now, as all parameters were estimated, an outgrowth trajectory was calculated for each iteration. This ensemble of trajectories was used to calculate the confidence intervals of the model prediction (Fig. 4C). The same approach was used for the model scenarios with individual cell mechanisms turned off (Fig. 4D-G). The source code is available in the supplementary notebook “lg\_model”.

## Coordinate system

Time starts with the event of amputation. For spatial positions along the AP axis of the spinal cord, the amputation plane defines 0; positive values refer to positions posterior to the amputation plane, in regenerated tissue; negative values refer to positions anterior to the amputation plane. In all images, anterior is to the left.

## Statistics and computational tools

If not stated otherwise, measurements are reported as mean  $\pm$  standard error of the mean. In the figures \* denotes  $p < 0.05$  and \*\* denotes  $p < 0.01$  for the respective test as indicated in the figure caption.

Image analysis was performed with Fiji (Schindelin *et al.*, 2012) and AxioVision Microscopy software (Zeiss). Data analysis was performed using the python modules bokeh (<http://bokeh.pydata.org>), iminuit (<http://github.com/iminuit/iminuit>), ipycache (<http://github.com/rossant/ipycache>), Jupyter Notebook (<http://jupyter.org/>), matplotlib (Hunter, 2007), numba (<http://numba.pydata.org/>), pandas (McKinney, 2010), probfit (<http://github.com/iminuit/probfit>), pymc (Patil *et al.*, 2010), SciPy (Jones *et al.*, 2001) and uncertainties (<http://pythonhosted.org/uncertainties/>).

## Supplementary notebooks

Jupyter Notebooks containing the source code for all computations performed together with the data and referred to as individually named supplementary notebooks in this work can be found under <http://dx.doi.org/10.5281/zenodo.58951>.

## Acknowledgements

We are grateful to Beate Gruhl, Sabine Mögel, Anja Wagner, and Heino Andreas for outstanding axolotl care. We thank Nuno Barros, Emanuel Cura Costa, Keisuke Ishihara, Jörn Starrauß and Anja Voß-Böhme for helpful discussions.

## Competing interests

The authors declare no competing interests.

## Author contributions

FR, Conception and design, Analysis and interpretation of data, Drafting or revising the article.  
ARA, Conception and design, Acquisition of data, Analysis and interpretation of data, Drafting or revising the article.  
VM, Acquisition of data, Drafting or revising the article.  
LB, Analysis and interpretation of data, Drafting or revising the article.  
AD, Drafting or revising the article.  
EMT, Conception and design, Analysis and interpretation of data, Drafting or revising the article.

529 OC, Conception and design, Analysis and interpretation of data, Drafting or revising the article.

## 530 **Funding**

531 This work was supported by grants from the Human Frontier Science Program (HFSP)  
532 RGP0016/2010, DFG-274/2-3/SFB655 'Cells into tissues', TU Dresden Graduate Academy  
533 (great!lipid4all) and the Center for Regenerative Therapies to E.M.T. and Agencia Nacional de  
534 Promoción Científica y Tecnológica (ANPCyT) PICT-2014-3469 'Mecanismos de Regeneración de la  
535 médula espinal del Axolotl: Una aproximación de Biología de Sistemas' to O.C. and BMBF grant  
536 (0316169A) to L.B. A.R.A. was funded by a DIGS-BB fellowship; F.R. and O.C. were funded by the  
537 HFSP, the German Ministry for Education and Research (BMBF, grant 0316169A) and TU Dresden  
538 Graduate Academy (great!lipid4all). O.C. is a career researcher from Consejo Nacional de  
539 Investigaciones Científicas y Técnicas (CONICET) of Argentina.

## 540 **References**

- 541 Becker CG, Becker T. 2015. Neuronal regeneration from ependymo-radial glial cells: cook, little Pot,  
542 cook! *Dev Cell*. **32**(4): 516-527. doi: 10.1016/j.devcel.2015.01.001.
- 543 Chara O, Tanaka EM, Brusch L. 2014. Mathematical modeling of regenerative processes. *Curr Top*  
544 *Dev Biol*. **108**: 283-317. doi: 10.1016/B978-0-12-391498-9.00011-5.
- 545 D'agostino R, Pearson ES. 1973. Tests for departure from normality. Empirical results for the  
546 distributions of  $b_2$  and  $\sqrt{b_1}$ . *Biometrika* **60**: 613–622. doi: 10.1093/biomet/60.3.613.
- 547 D'agostino RB. 1971. An omnibus test of normality for moderate and large size samples. *Biometrika*  
548 **58**: 341–348. doi: 10.1093/biomet/58.2.341.
- 549 Durant F, Lobo D, Hammelman J, Levin M. 2016. Physiological controls of large-scale patterning in  
550 planarian regeneration: a molecular and computational perspective on growth and form. *Regeneration*.  
551 **3**(2): 78-102. doi: 10.1002/reg2.54.
- 552 Echeverri K, Tanaka EM. 2003. Electroporation as a tool to study in vivo spinal cord regeneration. *Dev*  
553 *Dyn*. **226**(2): 418-25. doi: 10.1002/dvdy.10238.
- 554 Fei JF, Schuez M, Tazaki A, Taniguchi Y, Roensch K, Tanaka EM. 2014. CRISPR-mediated genomic  
555 deletion of Sox2 in the axolotl shows a requirement in spinal cord neural stem cell amplification during  
556 tail regeneration. *Stem Cell Reports*. **3**(3): 444-59. doi: 10.1016/j.stemcr.2014.06.018.
- 557 Gaete M, Muñoz R, Sánchez N, Tampe R, Moreno M, Contreras EG, Lee-Liu D, Larraín J. 2012.  
558 Spinal cord regeneration in *Xenopus* tadpoles proceeds through activation of Sox2-positive cells.  
559 *Neural Dev*. **7**:13. doi: 10.1186/1749-8104-7-13.

560 Greulich P, Simons BD. 2016. Dynamic heterogeneity as a strategy of stem cell self-renewal. *Proc*  
561 *Natl Acad Sci U S A.* **113**(27): 7509-14. doi: 10.1073/pnas.1602779113.

562 Holtzer SW. 1956. The inductive activity of the spinal cord in urodele tail regeneration. *J Morphol.* **99**:  
563 1-39. doi: 10.1002/jmor.1050990102.

564 Hui SP, Dutta A, Ghosh S. 2010. Cellular response after crush injury in adult zebrafish spinal cord.  
565 *Dev Dyn.* **239**(11): 2962-79. doi: 10.1002/dvdy.22438.

566 Hui SP, Nag TC, Ghosh S. 2015. Characterization of proliferating neural progenitors after spinal cord  
567 injury in adult zebrafish. *PLoS One.* **10**(12): e0143595. doi: 10.1371/journal.pone.0143595.

568 Hunter JD. 2007. Matplotlib: A 2D Graphics environment. *Comput Sci Eng.* **9**: 90–95. doi:  
569 10.1109/MCSE.2007.55.

570 Jones E, Oliphant T, Peterson P *et al.*, 2001. *SciPy: Open source scientific tools for Python.*  
571 <http://www.scipy.org/>

572 Kicheva A, Bollenbach T, Ribeiro A, Valle HP, Lovell-Badge R, Episkopou V, Briscoe J. 2014.  
573 Coordination of progenitor specification and growth in mouse and chick spinal cord. *Science.*  
574 **345**(6204): 1254927. doi: 10.1126/science.1254927.

575 Lacroix S, Hamilton LK, Vaugois A, Beaudoin S, Breault-Dugas C, Pineau I, Lévesque SA, Grégoire  
576 CA, Fernandes KJ. 2014. Central canal ependymal cells proliferate extensively in response to  
577 traumatic spinal cord injury but not demyelinating lesions. *PLoS One.* **9**(1):e85916. doi:  
578 10.1371/journal.pone.0085916.

579 Mchedlishvili L, Epperlein HH, Telzerow A, Tanaka EM. 2007. A clonal analysis of neural progenitors  
580 during axolotl spinal cord regeneration reveals evidence for both spatially restricted and multipotent  
581 progenitors. *Development.* **134**(11): 2083-93. doi: 10.1242/dev.02852.

582 McKinney W. 2010. Data structures for statistical computing in Python. In: van der Walt S & Millman J,  
583 editors. *Proceedings of the 9th Python in Science Conference.* p. 51–56.

584 Oates AC, Gorfinkiel N, González-Gaitán M, Heisenberg CP. 2009. Quantitative approaches in  
585 developmental biology. *Nat Rev Genet.* **10**(8): 517-30. doi: 10.1038/nrg2548.

586 Patil A, Huard D, Fonnesbeck CJ. 2010. PyMC: Bayesian stochastic modelling in Python. *J Stat Softw.*  
587 **35**: 1–81. doi: 10.18637/jss.v035.i04.

588 Rodrigo Albors A, Tazaki A, Rost F, Nowoshilow S, Chara O, Tanaka EM. 2015. Planar cell polarity-  
589 mediated induction of neural stem cell expansion during axolotl spinal cord regeneration. *eLife*  
590 e10230. doi: 10.7554/eLife.10230.

591 Rué P, Martinez Arias A. 2015. Cell dynamics and gene expression control in tissue homeostasis and  
592 development. *Mol Syst Biol.* **11**(1):792. doi: 10.15252/msb.20145549.

593 Schindelin J, Arganda-Carreras I, Frise E., Kaynig V, Longair M, Pietzsch T, Preibisch S, Rueden C,  
594 Saalfeld S, Schmid B, Tinevez JY, White DJ, Hartenstein V, Eliceiri K, Tomancak P, Cardona A. 2012.



595 Fiji: an open-source platform for biological-image analysis. *Nat Methods*. **9**: 676–682. doi:  
596 10.1038/nmeth.2019.

597 Smith C, Dendy PP. 1962. Relation between mitotic index, duration of mitosis, generation time and  
598 fraction of dividing cells in a cell population. *Nature* **193**: 555–556. doi: 10.1038/193555a0.

599 Sugiura T, Wang H, Barsacchi R, Simon A, Tanaka EM. 2016. MARCKS-like protein is an initiating  
600 molecule in axolotl appendage regeneration. *Nature*. **531**(7593): 237-40. doi: 10.1038/nature16974.

601 Tanaka EM, Ferretti P. 2009. Considering the evolution of regeneration in the central nervous system.  
602 *Nat Rev Neurosci*. **10**(10): 713-23. doi: 10.1038/nrn2707.

603

## Figure supplements

### Figure 1 – figure supplement 1

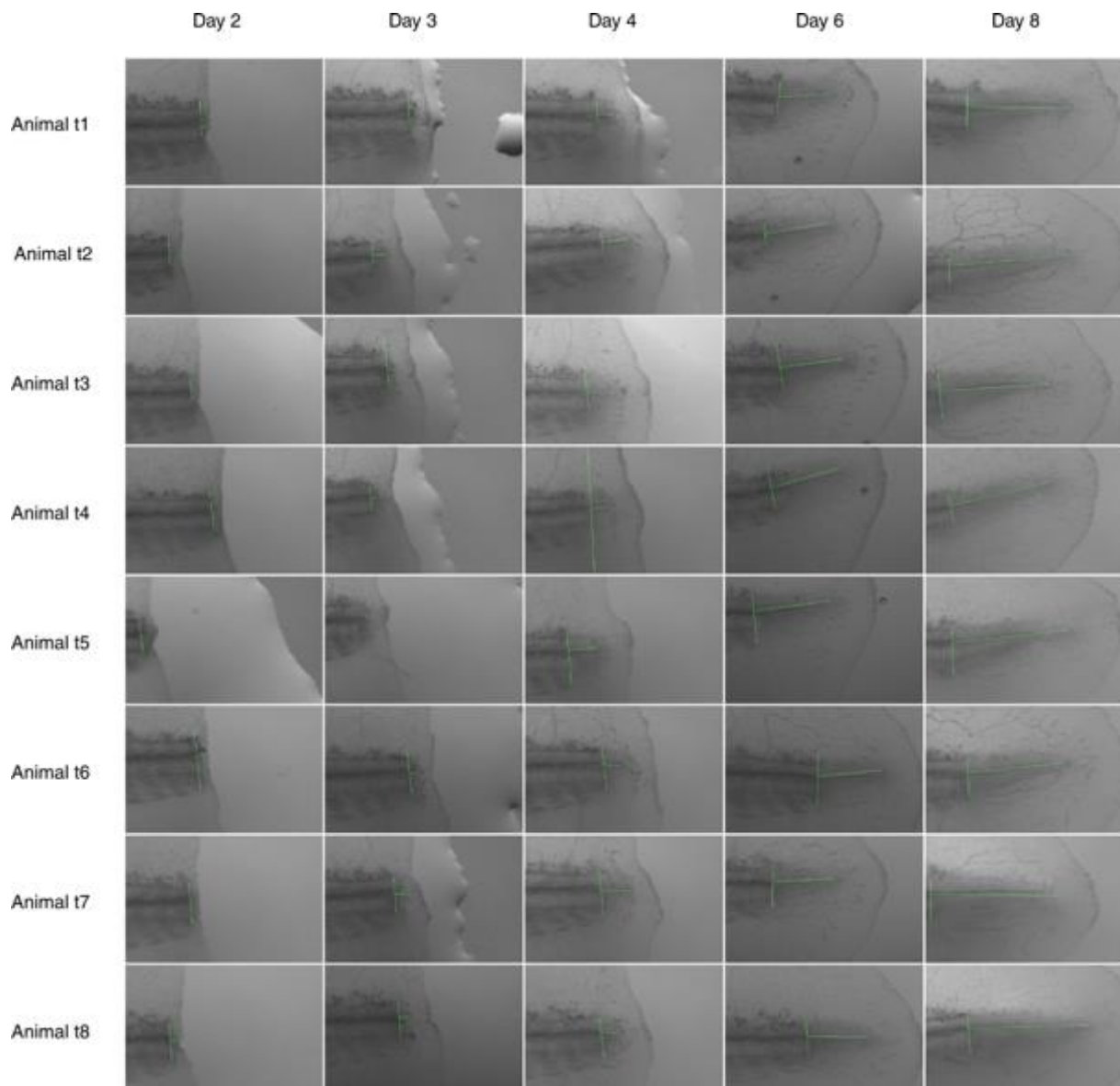


**Figure 1 – figure supplement 1.** Images used for spinal cord outgrowth measurements in Figure 1B. Each row shows images from an axolotl; each column shows animals from one time point analyzed. Vertical and horizontal lines mark the amputation plane and the spinal cord outgrowth, respectively. High-resolution images are in Supplementary file 1. Animal t3 is shown in the representative images of Figure 1A.

# Figure 2 – figure supplement 1

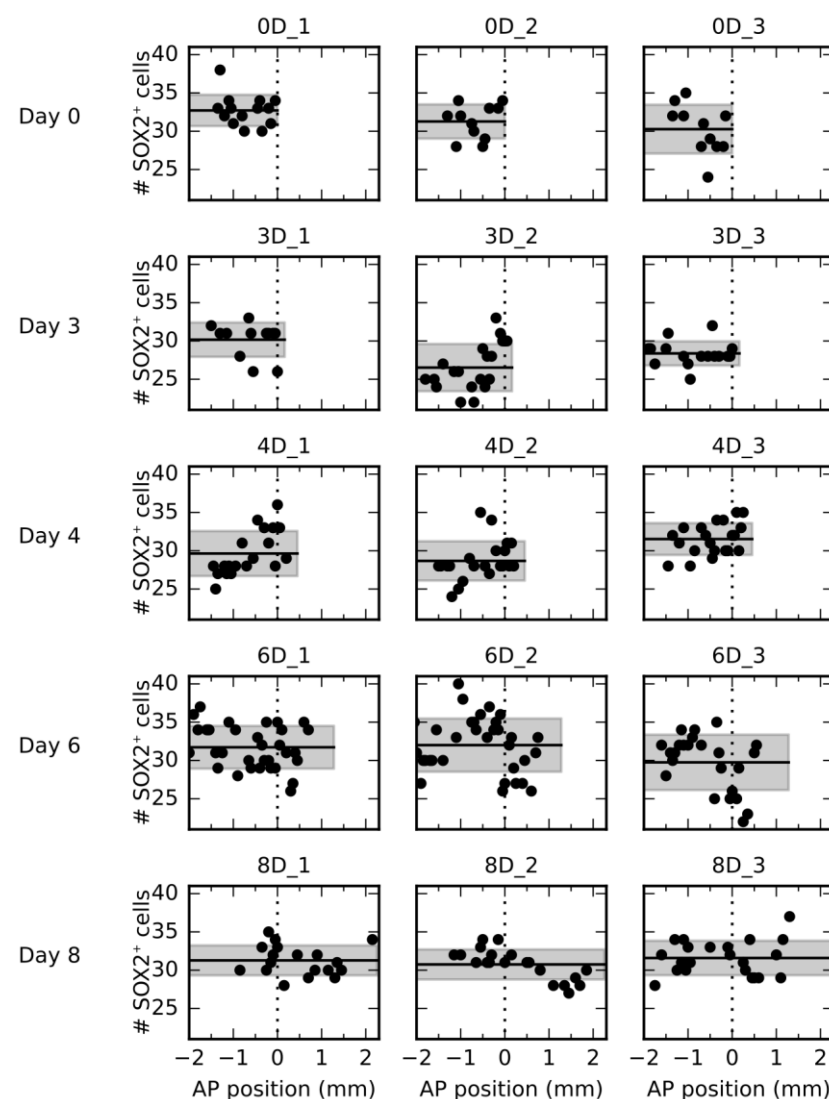


**Figure 2 – figure supplement 1.** Number of SOX2<sup>+</sup> cells per cross section along the AP axis for all 15 animals. Each row shows data from three animals at a given time point. Data from animals 0D\_1 and 4D\_3 are shown as representative data in Figure 2B and B', respectively.

# Figure 2 – figure supplement 2

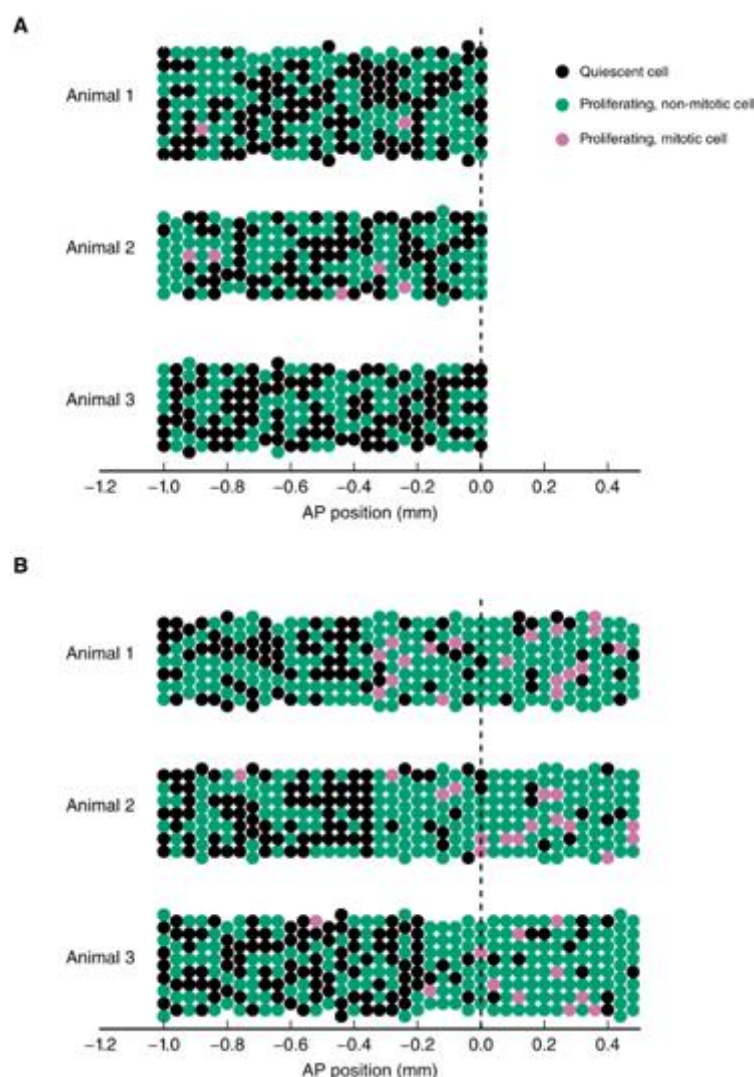


**Figure 2 – figure supplement 2.** Simulation of the spatial model of cell counts to analyze the spatiotemporal pattern of cell proliferation. (A) Simulations of a spatially homogeneous zone of proliferation for 3 animals. Population mean number of stem cells per cross section,  $NS_{pop} = 7$ , inter-animal standard deviation for number of stem cells per cross section,  $\sigma_{pop} = 1$ , intra-animal standard deviation number of stem cells per cross section,  $\sigma = 0.5$ , probability of a cell to be proliferating (expected growth fraction),  $p_p = 0.5$ , inter-animal standard deviation of  $p_p$ ,  $\sigma_p = 0.04$ , probability of a proliferating cell to be mitotic (expected mitotic index),  $p_m = 0.015$ , inter-animal standard deviation of  $p_m$ ,  $\sigma_m = 0.003$ . (B) Simulations of two adjacent spatially homogeneous zones of proliferation for 3 animals. Parameters for the anterior zone are the same as in (A). Probability of a cell to be proliferating and probability of a proliferating cell to be mitotic in the posterior zone are elevated to  $p_p = 0.8$  and  $p_m = 0.1$ , respectively. The mean switch point location is 300  $\mu\text{m}$  anterior to the amputation plane and the corresponding inter-animal standard deviation is 100  $\mu\text{m}$ . As expected, there are more proliferating and mitotic cells in the posterior zone. Simulation results can statistically be compared with the cell counts we obtained from experimentally observed animals to infer growth fraction, mitotic index and switch point (Figure 2F-F').

**Figure 2 – figure supplement 3**

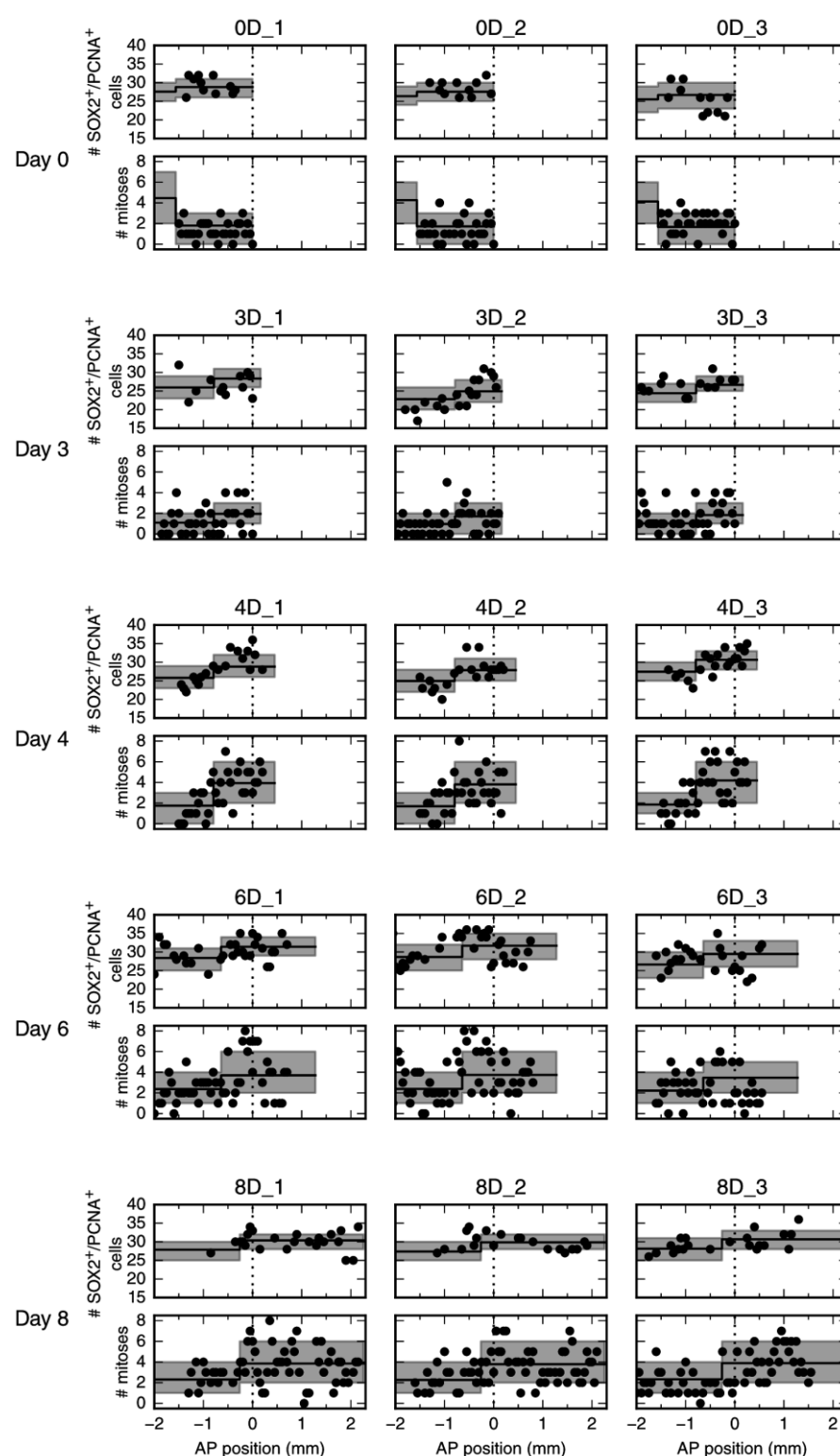
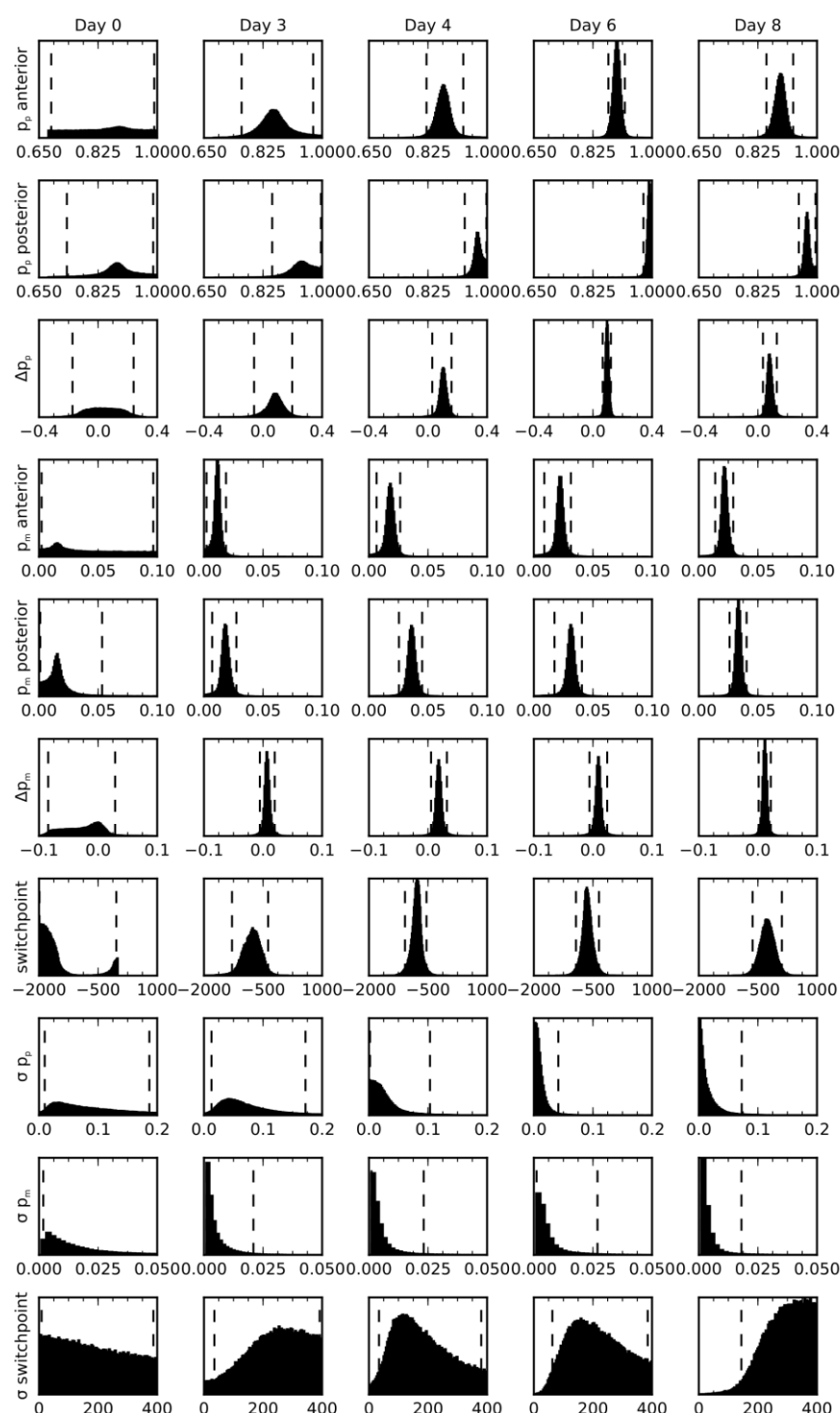


**Figure 2 – figure supplement 3.** Number of proliferating SOX2<sup>+</sup> cells per cross section (upper panel) and mitotic cells per section along the AP axis for all 15 animals. Data from animals 0D\_1 and 4D\_3 are shown in Figure 2E and 2E', respectively. Each row shows data from three animals at a given time point.

# 636 **Figure 2 – figure supplement 4**



637  
638 **Figure 2 – figure supplement 4.** Posterior marginal distributions for the parameters of the spatial model of cell  
639 counts to analyze the spatiotemporal pattern of proliferation. Each row shows a different model parameter. Each  
640 column shows a different time point. 3 animals per time point were used in the analysis. Vertical dashed lines show  
641 the limits of the 95% credibility interval. The distribution means and the 68% credibility intervals for the growth  
642 fraction, mitotic index and the switch point are shown in Figure 2F-F", respectively.

# **Figure 2 – figure supplement 5**

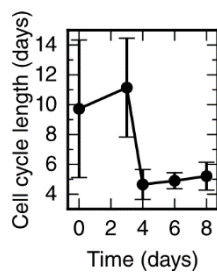


**Figure 2 – figure supplement 5.** Cell cycle length time-course calculated from the proliferation rate time-course shown in Figure 2G.



# Figure 3 – figure supplement 1

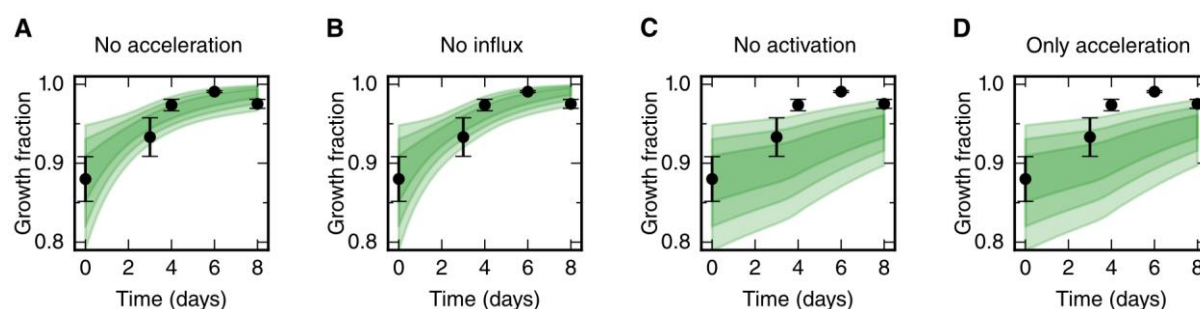


**Figure 3 – figure supplement 1.** Prediction of growth fraction in the high-proliferation zone for four model scenarios with selected mechanisms switched off (green shaded areas). Black dots show the same experimental data as in Figure 3B. Scenarios in panels A-D correspond to the scenarios in Figure 3D-G, respectively. Switching off the acceleration of the cell cycle length and switching off the cell influx hardly have an effect on the growth fraction time course (A,B). As expected, switching off the activation of quiescent stem cells has a strong impact on growth fraction time-course (C,D). This is consistent with the fit of a non-zero rate activation rate  $k$  to this data.

## **Additional files**

### **Supplementary file 1**

Stack of individual high-resolution images shown together in Figure 1 – figure supplement 1. Can be opened with Fiji or ImageJ.

### **Supplementary file 2**

Zip archive containing all raw images used for the clone tracking. The image files can be opened with AxioVision Microscopy software (Zeiss). Images for each individual animal are in separate folders. Folder names correspond to the animal IDs used in the clone trajectory dataset (see supplementary notebook “clone\_velocities”). The image filename indicates the time point of the measurement and the ID.